Annals of R.S.C.B., ISSN: 1583-6258, Vol. 25, Issue 1, 2021, Pages. 6096 - 6110
Received 15 December 2020; Accepted 05 January 2021.

An Efficient Automated 3D Lung Cancer Tumor Visualization and Volume Measurement using Simpleware Synopsys Toolkit

P.Samundeeswari[1*], R.Gunasundari[2]
[1]Research scholar, Electronics and Communication Engineering Department,
Pondicherry Engineering College, Puducherry, India.
[2]Professor, Electronics and Communication Engineering Department,
Pondicherry Engineering College, Puducherry, India.
[1]*samu@pec.edu, [2]gunasundari@pec.edu

ABSTRACT

Lung cancer is considered the deadliest disease all over the globe. Early diagnosis can reduce the mortality rate by 20%. Computed tomography (CT) is considered a precise imaging technique used for lung cancer diagnosis. Though CT slices have the features of high resolution, non-invasive, and painless, the availability of hundreds of two-dimensional lung CT slices makes the detection process difficult and might result in false alarms. Recently, 3D visualization diagnosis for lung cancer detection and segmentation becomes an interesting domain for physicians. The utilization of 3D visualization assists the doctors to observe the pulmonary nodules efficiently. Therefore, this paper develops an automated 3D lung cancer tumor visualization and volume measurement technique using Simpleware Synopsys software. The presented model uses Simpleware Synopsys software to visualize the tumor in 3D format and measure the tumor size. The presented model in Simpleware Synopsys software involves different processes such as preprocessing, segmentation, morphological operations, 3D tumor visualization, and tumor volume measurement. The presented model uses Median Filtering (MF) as a preprocessing technique to remove the noise. In addition, region growing based segmentation technique is used to detect the tumor regions accurately. Besides, a set of morphological operations such as erode, dilate, open, and close are utilized. To examine the effective performance of the presented method, extensive experimentation was carried out on LIDC dataset and our own dataset collected from JIPMER hospital, Puducherry, India. The simulation outcome ensured the superior performance of the presented model by obtaining a maximum 3D visualization accuracy of 98% which is nearly 3.80% more than the existing methods.

Keywords
Lung cancer; 3D visualization; Synopsys software; Disease diagnosis; Computed tomography.

Introduction

Globally, lung cancer is found to be a deadly disease among all other cancer types [1]. There are many reasons for lung cancer and one among them is smoking habit. In addition, alcohol and tobacco consumption, frequent pollution are also the most common reasons for lung cancer which affects both males and females. Even though direct exposure to tobacco consumption is a major risk factor, breathing unwanted carcinogens by marijuana or hookah is also a significant cause of lung cancer. Some other risk factors are exposure to radon, asbestos, diesel exhaustion, and ionizing radiation. Based on the survey, a correlation between lung cancer and chronic obstructive lung disease which are independent of tobacco consumption and possibly arbitrated by hereditary disorder [2]. Even non-smokers and tea-tootler are affected by lung cancer, which

represents a possibility of these cases and treated with some oncogenic modifications and individualized medications.

A pathological analysis has to be developed with World Health Organization (WHO) classification since the effective treatment procedures are computed according to the histologic characteristics. Lung cancer is classified into Small-Cell Lung Cancer (SCLC) and Non–SCLC (NSCLC). When the lung cancer is predicted by using various medical devices or cytologic instance represents unambiguous morphologic property of adenocarcinoma or squamouscell carcinoma, the diagnosis has to be performed effectively and, immunocytochemical or immunohistochemical investigation is not required. When morphologic estimation shows neuroendocrine features, a tumor is categorized as SCLC and NSCLC. When the morphologic features are unclear, the tumor is divided into NSCLC, and Not Otherwise Specified (NOS). When the class of tumors is NSCLC, NOS is more classified on the basis of immunocytochemical or immunohistochemical examination, mucin staining, or molecular details.

Computed Tomography (CT) is one of the well-known and effective imaging mechanism used to screen the actual position of a lesion. Alternatively, Positron-Emission Tomography with CT (PET-CT) and Magnetic Resonance Imaging (MRI) is the imaging modalities utilized for enhancing the accuracy of baseline performance and tends to make robust and exact estimation of response to treatment [3]. Even though the outcomes are statistically same, every sample owns specific advantages. MRI performs well than PET-CT with respect to brain imagining and liver metastases, while PET-CT performs well than MRI by means of estimating lymph nodes and soft tissues. Therefore, although non-invasive imaging is applicable, tissue analysis is meant to be essential process to predict the existence of lung cancer and observe the treatment response.

The earlier prediction of lung cancer is a significant process. The commonly used models for lung cancer prediction are scrutinizing the clinical chest image. Typically, CT is a precise imaging method used for scanning the lung disease [4]. CT slices are composed of the features like maximum resolution, non-invasive, and painless, which play a vital role in earlier screening of lung diseases. Therefore, chest CT is comprised of numerous 2D scans. When lung cancer screening is processed, there are maximum chances of misclassifications due to the presence of maximum CT slices. Therefore, it can be essential to establish a Computer-Aided Diagnosis (CAD) approach is capable of predicting the disease automatically and guides in observing the pulmonary nodules [5]. Using the advanced 3D technology, recently developed high definition (HD) imaging models provide better image quality and resolution, as same as 2D. Various studies have represented the merits of 3D-HD over traditional 2D HD by means of enhancing surgeon process in reputed skills.

This paper introduces a novel automated 3D lung cancer tumor visualization and volume measurement technique using Simpleware Synopsys software. The presented model makes use of Simpleware Synopsys software to visualize the tumor in 3D format and measure the tumor size. The presented model in simpleware Synopsys software involves different processes such as preprocessing, segmentation, morphological operations, 3D tumor visualization, and tumor volume measurement. In order to examine the effective performance of the presented model, extensive experimentation was carried out on LIDC dataset and our own dataset collected from JIPMER hospital.

Annals of R.S.C.B., ISSN: 1583-6258, Vol. 25, Issue 1, 2021, Pages. 6096 - 6110
Received 15 December 2020; Accepted 05 January 2021.

Related works

Classical auxiliary diagnosis involves pre-processing, lung segmentation, Region of Interest (RoI) prediction, feature extraction, Feature Selection (FS), classification, False Positive (FP) limitation, and so on [6]. Deployment of Deep Learning (DL), parametric Rectified Linear Unit Nets (PReLU-nets) has outperformed manual performance on visual analysis [7]. Followed by, some researchers have deployed object prediction and segmentation methodologies based on DL as pulmonary nodule prediction. [8] predicted the sensitivity of FP per scan with the help of multi-view structure on LIDC-IDRI dataset [9]. In 3D Convolutional Neural Networks (3D CNN) for FP limitation and achieved Competition Performance Metric (CPM) value. Moreover, the volume measurement is performed by the segmentation of pulmonary nodules.

[10] computed segmentation and classification processes of lung masses from CT under the application of k-means clustering method. However, this model is capable of predicting lung cancer with large and small nodules. [11] presented a mask region CNN (Mask R-CNN) which is defined as a multitasking system and simulates prediction and segmentation simultaneously. Hence, there are numerous hyper-parameters for optimizing various operations.

[12] expanded Mask R-CNN by merging FPN to enhance the precision of small-scale segmentation. Even though the accuracy is enhanced in small object prediction, it fails in case of large object prediction. Besides, it is applicable for auxiliary estimation and to provide better treatment while segmentation results are envisaged as 3D modules [13]. Nowadays, 3D examination of clinical images is still in progress and concluded with better efficiency. Levy presented a volume rendering model for displaying the surface by ray-casting [14], where 3D model and interior details are viewed and argued. Therefore, processing complexity and memory space are essential. In [15], the robustness of ray-casting model has been simulated using parallel computing. When compared with classical approach, the computational complexity of the newly developed ray-casting model is reduced to a greater extent.

[16] has developed a new Volumetric Analysis Framework for Accurate Segmentation and Classification (VAF-ASC) for lung tumor diagnosis. The volumetric analysis model contains the determination of length, thickness, and height of the identified tumor cell to achieve effective outcome. It performs segmentation using optimal thresholding and morphological functions. Besides, k-means clustering technique is applied to form clusters depending upon background imaging, images with soft muscles, and tumor cells with large airways, based on the gray scale evaluation. Though several models are available in the literature, there is still needed to develop an effective detection and classification model.

Proposed Model

The working principle involved in the proposed model is shown in Figure 1. As said earlier, we have used Simpleware Synopsys software for lung tumor 3D visualization and volume measurement. The set of processes used in the applied software are median filtering (MF) based pre-processing, region growing based segmentation, morphological operations, smoothing, cavity filling, fill gaps, island removal, and local surface correction. By the use of these processes, the lung tumor can be visualization and the volume can also be determined. Primarily, the input image undergoes noise removal process using MF technique. Afterward, the region growing technique is applied for segmenting the preprocessed image. Followed by, morphological

Annals of R.S.C.B., ISSN: 1583-6258, Vol. 25, Issue 1, 2021, Pages. 6096 - 6110
Received 15 December 2020; Accepted 05 January 2021.

operations are carried out and then MF is applied for smoothening the resultant image. Consequently, cavity fill process takes place to fill the outer walls and fill gaps process is carried out to fill the holes. Next to that, the island removal process is carried out to remove the small regions, i.e., the region size ≥ 3 is considered as a tumor and the regions with <3cm are ignored. Simultaneously, local surface correction process gets executed. At last, the tumor can be visualized in a 3D way and the volume of the tumor can also be determined.

Synopsis Software

Here, 3D datasets are processed with the help of lucrative third-party software named Synopsis developed by Simpleware. Moreover, this software is utilized in calculating the volume of the lung tumor liver by examining the pixel count marked inside the liver region using segmentation model. Followed by, inputs are induced into the software are segmented dataset and actual resolution of CT datasets are performed. Thus, the volumes are measured in Milliliters (mL).

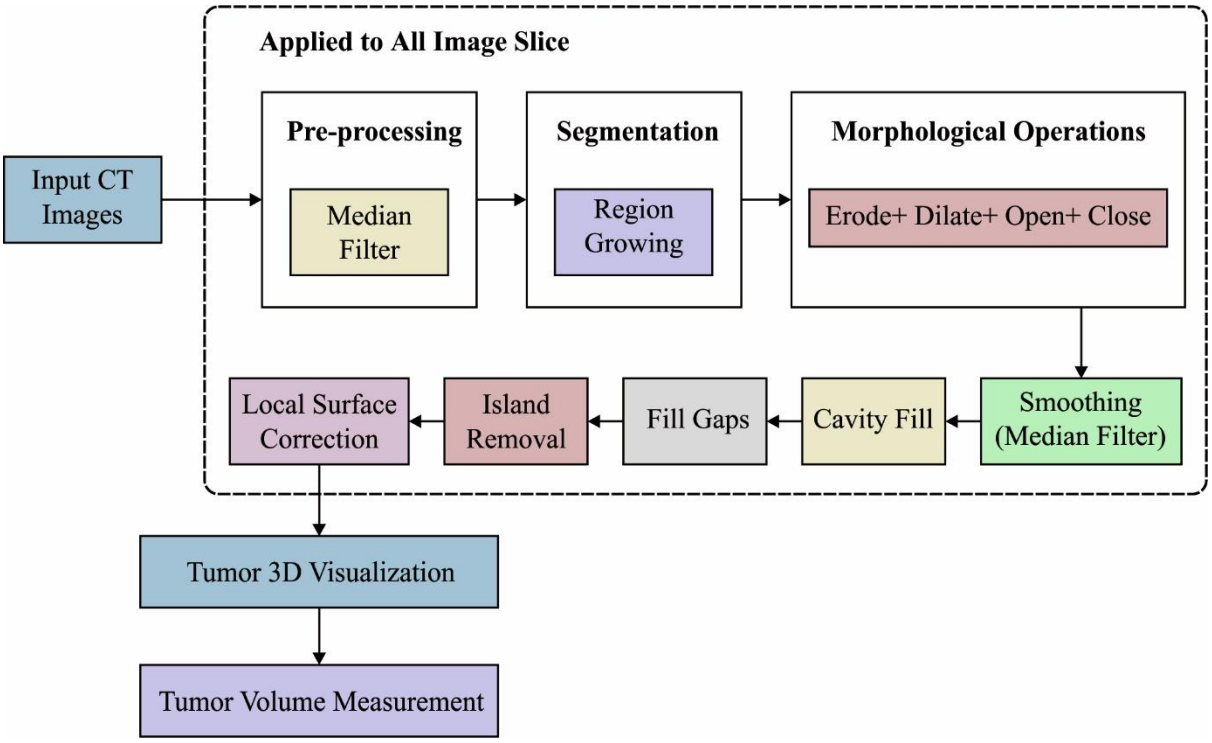

Figure 1. Block diagram of proposed model

Preprocessing

MF method is a non-linear signal processing method. The irregular digital image is extended using median value of adjacent value which is also called a mask. The pixels are ranked for gray levels, and median value of a group is secured for replacing the wrong value. Hence, the simulation outcome of MF is illustrated as $g(x,y) = med\{f(x-i, y-j), i, j \in W\}$, where $f(x,y), g(x,y)$ defines the original and consequent images respectively, W implies 2D mask: with a size of $n \times n$ in which $3 \times 3, 5 \times 5$, etc. A mask has various structures like linear, square, circular, cross, and so on. Since the MF belongs to a non-linear filter, mathematically investigation is not possible for an image with random noise. If an image is allocated with zero mean, noise below normal distribution, and noise variance of MF is expressed as,

Annals of R.S.C.B., ISSN: 1583-6258, Vol. 25, Issue 1, 2021, Pages. 6096 - 6110
Received 15 December 2020; Accepted 05 January 2021.

$$\sigma_{med}^2 = \frac{1}{4nf^2\overline{(n)}} \approx \frac{\sigma_i^2}{n + \frac{\pi}{2} - 1} \cdot \frac{\pi}{2} \quad (1)$$

Where σ_i^2 implies the input noise power, n defined the MF size, $f\overline{(n)}$ indicates the function of noise intensity. Besides, noise variance of average filtering is represented by,

$$\sigma_0^2 = \frac{1}{n}\sigma_i^2 \quad (2)$$

From the comparison results of (1) and (2), MF functions have relied on 2 objectives like size of a mask and noise distribution. The main goal of MF is to eliminate the noise with acceptable efficiency than average filtering, Therefore, in case of impulse noise, and narrow pulses are away, and also if pulse width is minimum than $n/2$, then MF becomes more efficient. The aim of MF is to increase the performance when MF model is combined with average filtering scheme.

Region growing based Segmentation

The image is sliced into 2 regions like background and foreground, with the help of region growing model. This is accomplished by selecting seed and extend them. Assume that $x \in$ I is a randomly selected pixel from 2D image II. Assume that R_f is an ROI of an image I, referred as foreground, and δ_1 implies the tolerance of variations in intensity. Also, a simple method to extend R_f is to compare the neighborhood pixels with basic seed and allocate each pixel to R_f when it meets the condition given below:

$$|x - N(p)| \leq \delta_1 \quad (3)$$

where $N(p) \in$ I define a neighborhood pixel of R_F and $|.|$ denotes the absolute variation of intensity. If a pixel is allocated to R_f, then new neighborhood pixel is measured similarly. But, if a noise pixel has been selected, undesirable outcome might be generated. Alternatively, the pixel from external region is compared with nearby neighborhood pixel. It is same as Eq. (3); however, comparing $N(p)$ and external pixel of R_F, is expressed as $S(x)$:

$$|S(x) - N(p)| \leq \delta_2 \quad (4)$$

The initial method results in reliable segmented regions; but is sensible to noise whereas the second model results in irregular segmentation, in particular, if the pixel attributes are changed gradually, but it overcomes the noisy inputs. Multiple-seeds are considered to be an alternative to resolve the predefined problems. The initialization is composed of multiple pixels; however small set of pixels defines the region with the help of statistical devices like mean or variance. Followed by, expansion is contributed by statistic expression. Therefore, it is costlier since a neighborhood pixel is estimated as multiple pixels. These models are combined by changing the multiple-seeds as a way to gain a ground truth measure of RoI.

In order to manage the case if the selected pixel is non-representation of the region, then a median of multiple-seeds can be measured. For instance, both initializations result in 34. Next, the expansion applies Eq. (3) and Eq. (4) and allocate a measure $\delta_1 > \delta_2$. Eq. (3) retains the reliability of segmented regions and Eq. (4) removes a jump transition. It is essential in noise reduction, and blurring is employed for the image. Here, the blurring image by Gaussian tends to accomplish optimal segmentation. Steps involved in the region growing algorithm are listed in the following:

1. Click mouse in the RoI.
2. Select N × N neighborhoods. It is clear that basic seed point has to be placed in the middle portion and N should be an odd number.

Annals of R.S.C.B., ISSN: 1583-6258, Vol. 25, Issue 1, 2021, Pages. 6096 - 6110
Received 15 December 2020; Accepted 05 January 2021.

3. Fix the primary value for overall pixels in a region with 1 and grey level for every pixel in a region with actual grey level value of basic seed pixel.
4. Estimate the mean value, x that is named as region mean as well as Standard Deviation (SD), σ of N × N neighborhood.
5. Develop seed pixels to the neighbor's pixels. Relate the grey level of seed pixel with corresponding neighbor's pixel. A neighbor pixel is placed within a region when it satisfies maximum conditions given in the following:
   - When gradient of the pixel is minimum than 95% of equalized histogram and the grey level of pixel is less than or equivalent to existing threshold.
   - When the gradient of pixel is maximum than 95% of equalized histogram and grey level of the pixel is less than SD from the region means.
6. When the neighbor pixel is added within the region:
   - Include one (1) to overall pixels in a region value.
   - Include actual grey level of neighbor pixel to overall grey level for pixels in a region value.
7. Fix the neighboring pixel that is then included in the region in Step (5) and referred as novel seed pixel.
8. Follow steps (4) to (7) till reaching the developed pixels. Estimate the value of size and grey level of a region.

Morphological Operations

Some of the morphological operators are dilated, erode, open, and close which are employed by image filtering to add or delete the image regions and to eliminate or occupy the image region boundary pixels. The fundamental operators which proceed the objects from the input image on the basis of features encoded in decided structuring component as defined in the following:

Dilate and Erode

Dilation and erosion are the fundamental operators in numerical morphology. A major purpose of dilation on an image is for magnifying the edges of the regions in foreground pixels, especially the white pixels. Since the regions of foreground pixels develop in size, the holes inside these regions become tiny. While the common impact of erosion on an image is to erode or degrade the boundaries of regions in foreground pixels. As same as dilation, the foreground pixels are reduced in size, and holes inside these regions are progressive. Also, dilation is applied for edge prediction by considering the dilation of an image and eliminate the actual image, where the new pixels from the edges are included by using dilation. Similarly, erosion is employed for edge forecasting under the assumption of image erosion and remove the actual image. It highlights the pixels from the edges of objects which are subtracted by erosion.
These 2 operators are computed on 2 inputs; initially, the image has to be dilated or eroded and secondly, a set of coordinate points are named as structuring element or kernel. The structuring element estimates the accurate impact of dilation or erosion an input image. The impact of dilation and erosion by 3x3 square structuring unit on binary image is depicted below. This structural element is one of the common modules applied in dilation and erosion process. Maximum structuring elements generated maximum impacts. Using the massive structuring elements, the round-shaped structuring element is applied which is the inverse square element.

Annals of R.S.C.B., ISSN: 1583-6258, Vol. 25, Issue 1, 2021, Pages. 6096 - 6110
Received 15 December 2020; Accepted 05 January 2021.

Open

The opening process is retrieved from basic morphological operations of erosion and dilation. The common impact of opening is less the erosion process that intends to eliminate the foreground (bright) pixels from edges of regions from foreground pixels. Generally, it causes minimum side effects when compared with erosion. Then, précised operation is estimated by using a structuring element. Hence, the key objective of this operator is to conserve the foreground regions with identical shape of structuring element at the time of removing other regions from foreground pixels.

Close

The closing process is the reverse method of opening which is defined simply as dilation and erosion by applying the same structuring element. Closing resembles dilation in few methods that tend to develop the edges of foreground regions in an image and occupy the tiny background holes called *pepper noise*. Therefore, it destructs the actual boundary shape. Since the morphological operators are employed, actual performance is evaluated by the structuring element. But, the impact of an operator is for conserving the background regions with identical shapes to the structuring element and remove the background pixels.

Resultsand performance validation

The simulation of the proposed model takes place using Simpleware Synopsys software is discussed here. The presented model has been validated using LICD-IDRI dataset [17] and JIPMER dataset. The first LIDC-IDRI dataset includes images of 100 patients with 150-400 images for each patient. The second JIPMER dataset comprises 10 patients with 120-300 images per patient. The information related to the dataset is given in Table 1 and the sample test images are illustrated in Figure 2.

Table 1. Dataset Descriptions

Dataset	**No. of Patients**	**No. of Images Per Patient**
LIDC-IDRI	100	150-400
JIPMER	10	120-300

Annals of R.S.C.B., ISSN: 1583-6258, Vol. 25, Issue 1, 2021, Pages. 6096 - 6110
Received 15 December 2020; Accepted 05 January 2021.

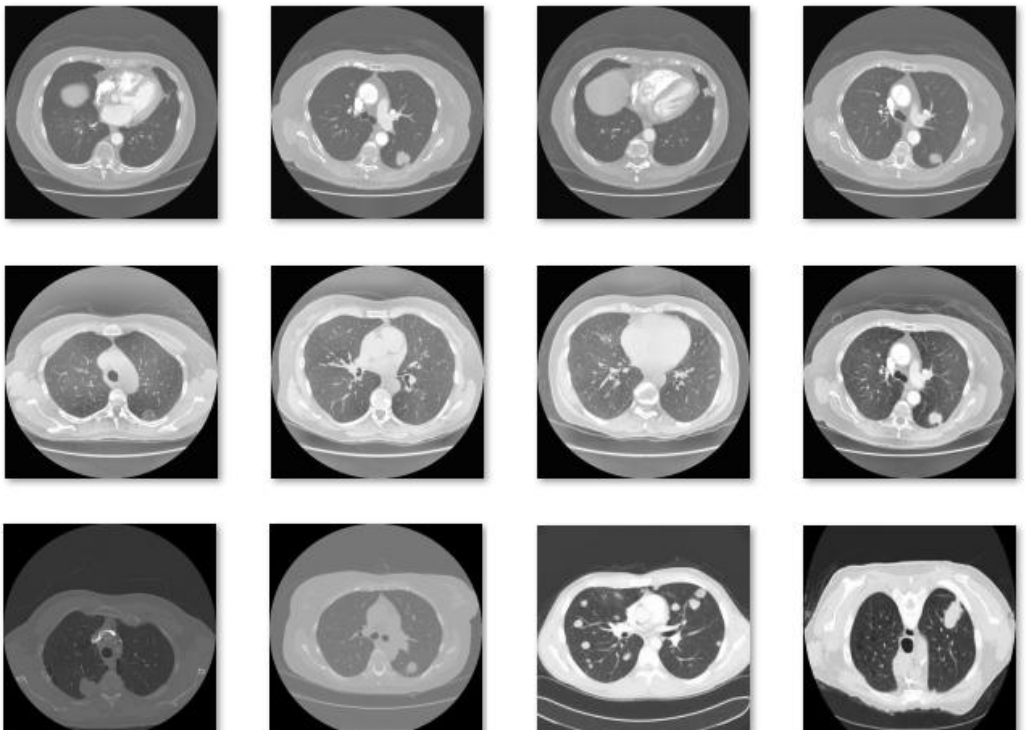

Figure2. Sample CT Images

Annals of R.S.C.B., ISSN: 1583-6258, Vol. 25, Issue 1, 2021, Pages. 6096 - 6110
Received 15 December 2020; Accepted 05 January 2021.

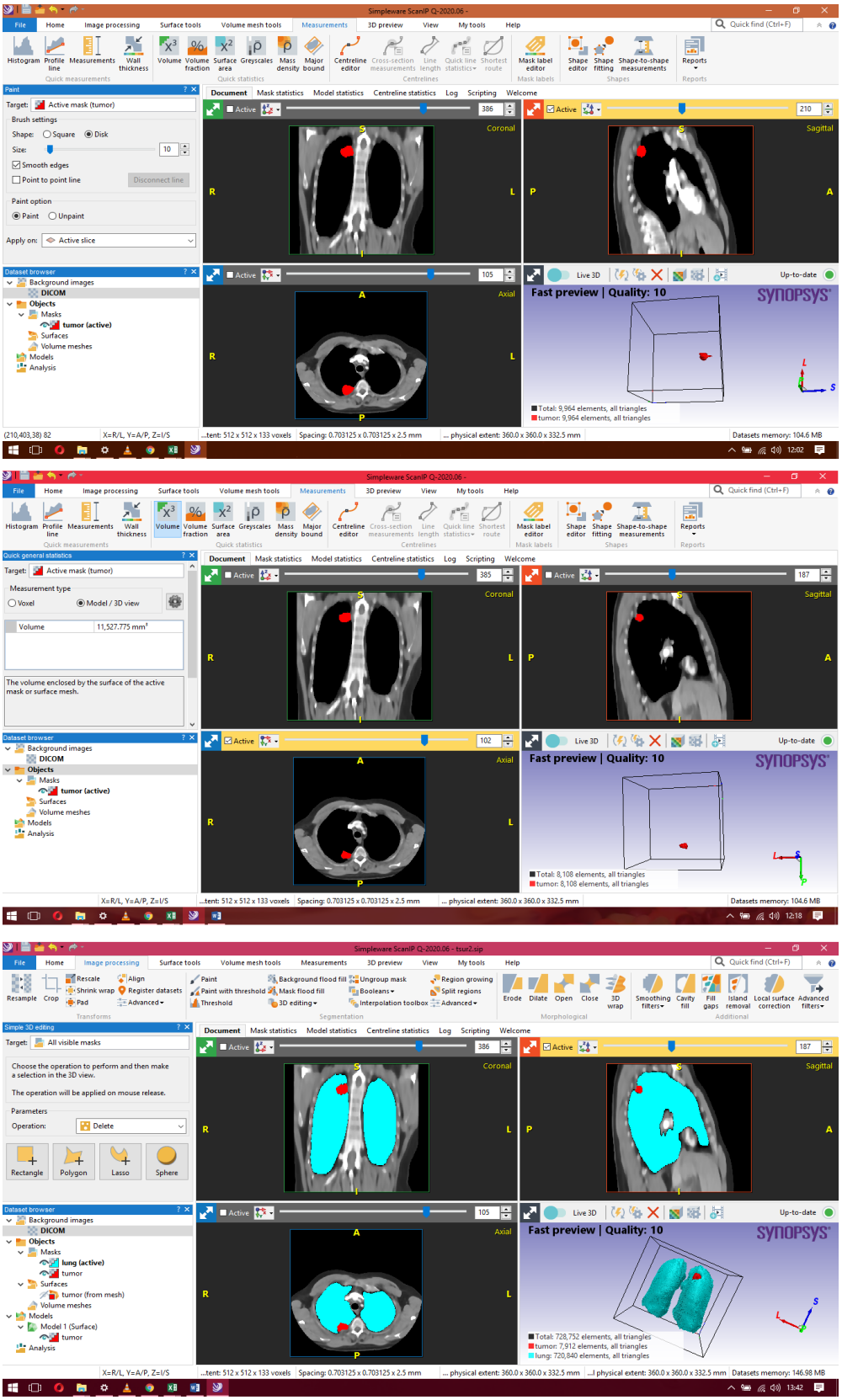

Figure 3. Sample 1-3D Visualization of LIDC IDRI IMAGE-022

Annals of R.S.C.B., ISSN: 1583-6258, Vol. 25, Issue 1, 2021, Pages. 6096 - 6110
Received 15 December 2020; Accepted 05 January 2021.

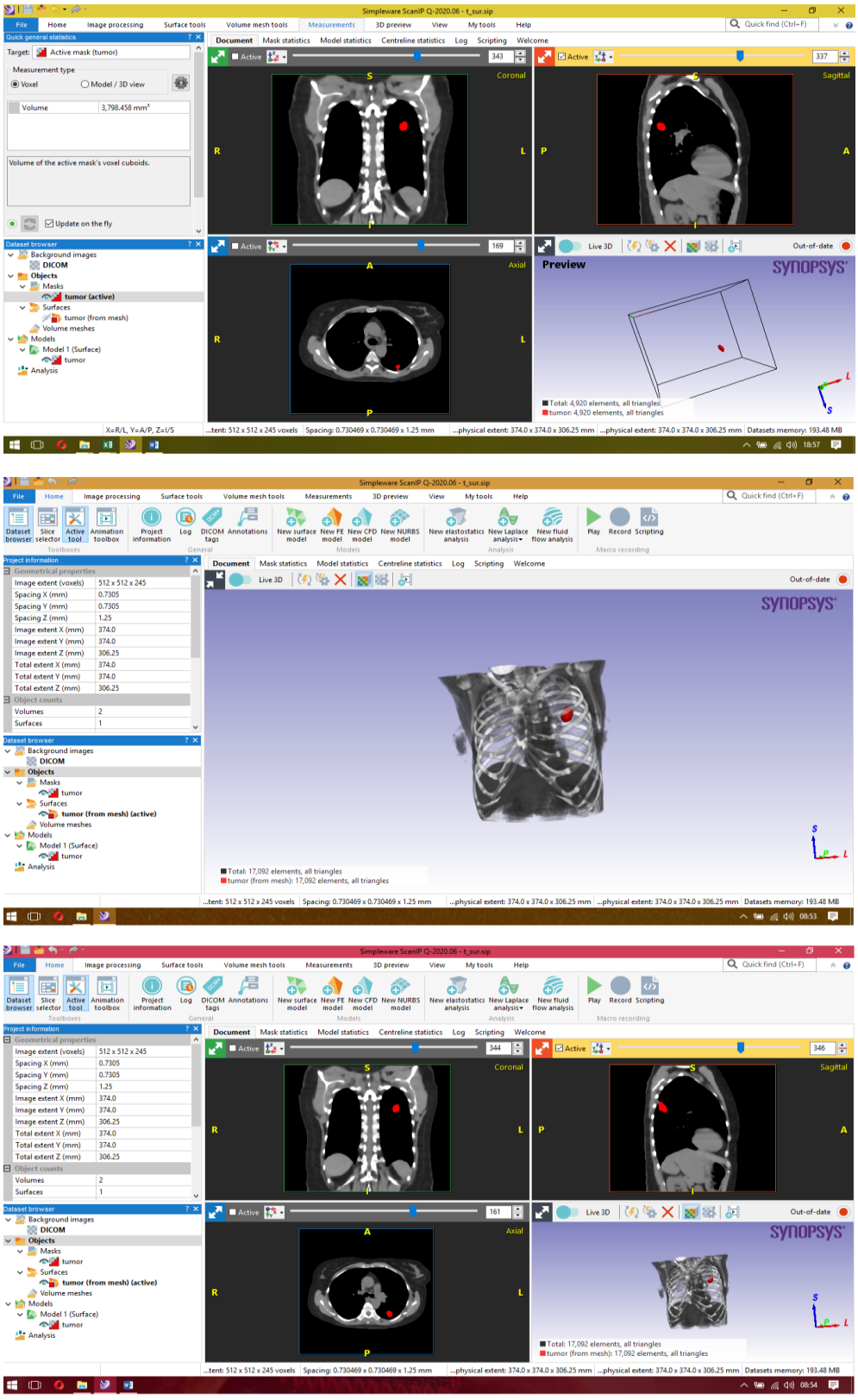

Figure 4. Sample 2-3D Visualization of LIDC IDRI IMAGE-057

Annals of R.S.C.B., ISSN: 1583-6258, Vol. 25, Issue 1, 2021, Pages. 6096 - 6110
Received 15 December 2020; Accepted 05 January 2021.

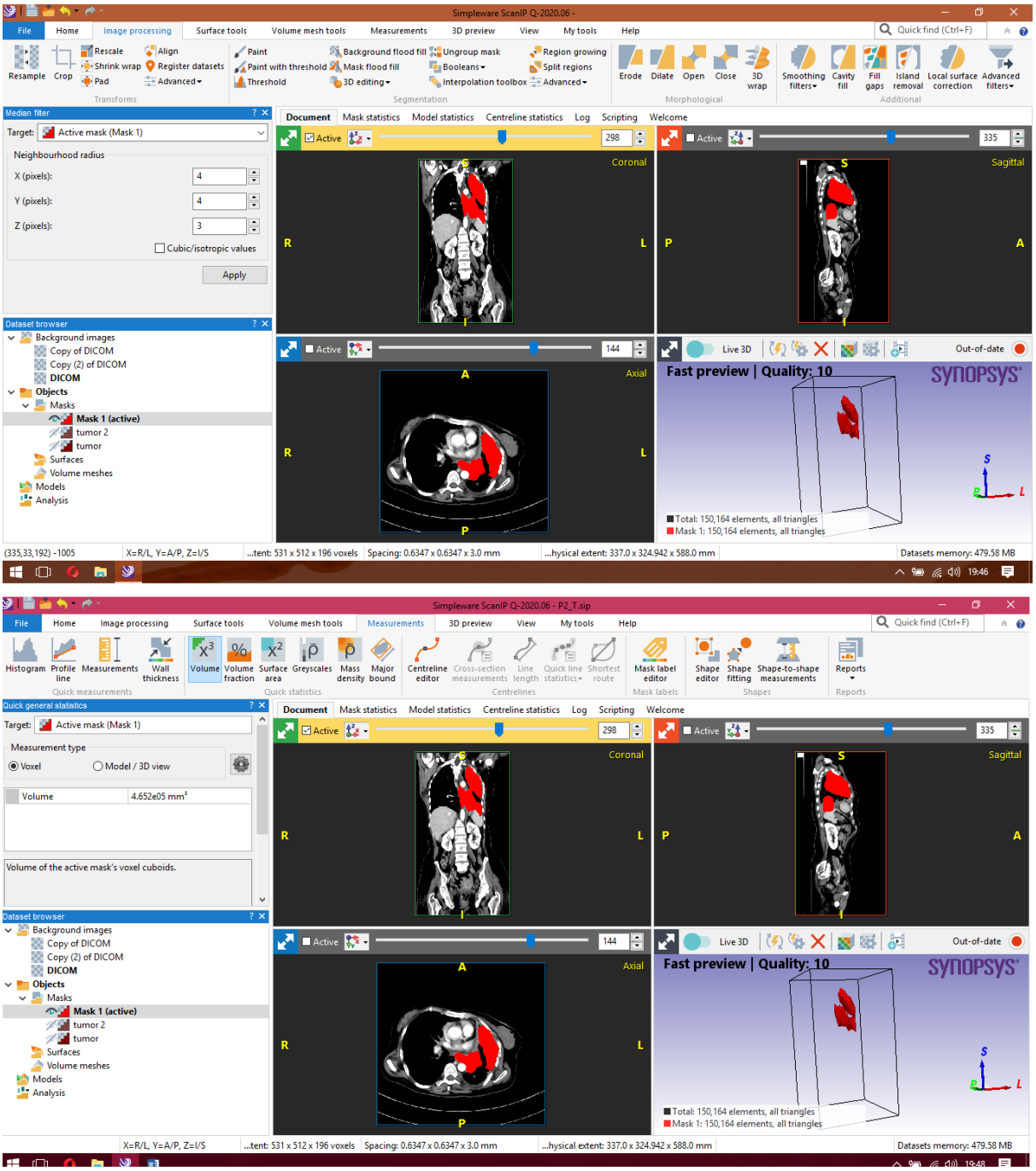

Figure 5. Sample 3-3D Visualization of JIPMER IMAGE

Similarly, Figure 3 shows the sample 3D visualization of image 022 on the applied LIDC IDRI dataset. From the figure, it is evident that the presented model has detected the tumor and visualized clearly in a 3D format. Likewise, Figure 4 showcases the sample 3D visualization of an image 057 on the applied LIDC IDRI dataset. From the figure, it can be clear that the presented model has predicted the tumor and examined clearly in 3D form. Figure 5 implies the sample 3D visualization of the sample image on the given JIPMER dataset. From the figure, it is apparent that the developed model has examined the tumor and visualized clearly in a 3D format.

Annals of R.S.C.B., ISSN: 1583-6258, Vol. 25, Issue 1, 2021, Pages. 6096 - 6110
Received 15 December 2020; Accepted 05 January 2021.

Sample Patients id number (LIDC-IDRI dataset)	Number of nodules	Volume determined by 4 radiologist (available in LIDC-IDRI dataset) mm^3	Volume determined by the proposed method in mm^3	Volume Measurement Difference (VMD) %
022	1	11672.42	11527.775	+1.2
029	1	5740.46	5636.891	+1.8
050	1	7657.62	7543.73	+1.48
052	2	1756.67	1791.3	-1.97
053	2	6239.75	6132.54	+1.7
054	1	2043.15	2002.56	+1.98
057	1	3737.10	3698.458	+1.03
081	2	3592.92	3524.13	+1.91
089	1	8424.86	8439.84	-1.67
094	1	3368.29	3309.84	+1.73

Table 2. Volume Measurement Difference for LIDC-IDRI Image dataset

Tables 2 and 3 demonstrate the tumor volume measurement results of the presented model on the applied test LIDC-IDRI and JIPMER image dataset. From the results, it is evident that the presented model has determined the tumor size correctly with a maximum difference of $\pm 2\%$ between the experimental results and experts' decision. For instance, on the applied sample id number 022 on the LICD-IDRI dataset, a tumor size of 11527.775 mm^3 has been determined by the presented model and the expert's measured the volume size of 11627.2 mm^3, indicating the difference of +1.2%. Likewise, on the given image-057, a tumor size of 3798.458mm^3 has been estimated by using newly developed approach and the experts have calculated the volume size of 3737.10 mm^3, representing the variations of +1.03%. Likewise, the presented model effectively determines the tumor volume on all the applied samples. Finally, on the applied patient id 1 on the JIPMER dataset, a tumor size of 5789.24mm^3 has been evaluated by the projected model and the expert's measured the volume size of 5726.14mm^3, implying the difference of +1.08%.

Table 3. Volume Measurement Difference for JIPMER Image dataset

Number of patients (JIPMER dataset)	Volume determined by radiologist mm^3	Volume determined by the proposed method in mm^3	Volume Measurement Difference (VMD) %
1	5789.24	5726.14	+1.08
2	3683.17	3740.56	-1.55
3	569.23	558.12	+1.95
4	2168.28	2128.65	+1.82
5	842.96	829.15	+1.63
6	4256.75	4213.05	+1.02
7	1563.54	1582.79	-1.23
8	2489.46	2443.13	+1.86

Annals of R.S.C.B., ISSN: 1583-6258, Vol. 25, Issue 1, 2021, Pages. 6096 - 6110
Received 15 December 2020; Accepted 05 January 2021.

9	3974.58	4004.73	-0.75
10	1784.46	1753.19	+1.75

Table 4 and Figure 6 investigates the detection results of the presented model with existing techniques [16] such as VAF-ASC, Massive Training Artificial Neural Networks (MTANN) and Genetic Algorithm-based Template Matching (GATM) models interms accuracy. On determining the results interms of accuracy, the existing MTANN model has obtained a lower classification outcome with a minimum accuracy of 74%. Simultaneously, the GATM model has demonstrated somewhat better accuracy value of 83%. At the same time, the VAF-ASC model has illustrated a moderate accuracy of 94.20%. However, the presented model has attained a superior accuracy of 98%.

Table 4. Performance comparison for volumetric analysis

S. No	Methods	Average Volume Accuracy (%)
1	MTANN	74.00
2	GATM	83.00
3	VAF-ASC	94.20
4	Proposed method	98.00

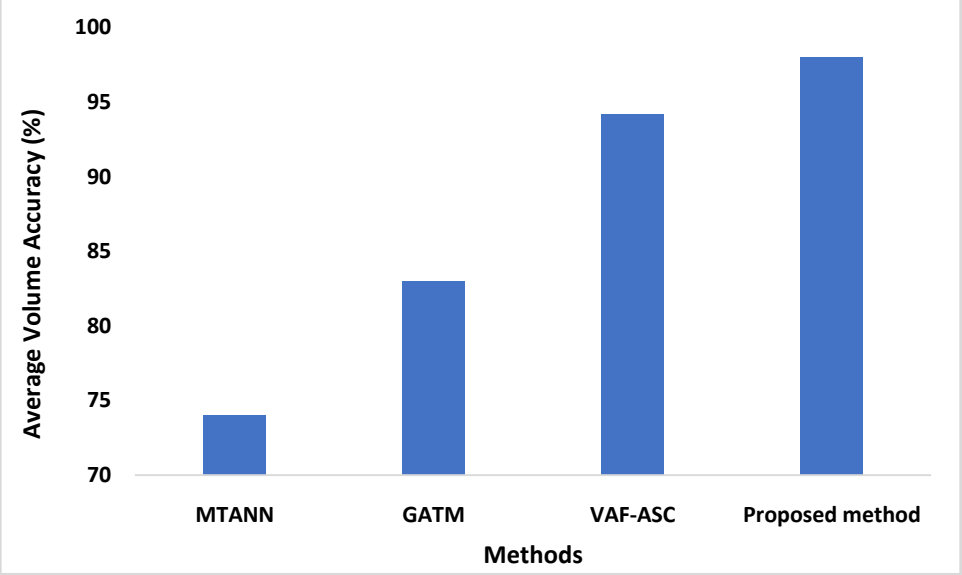

Figure 6. Comparative analysis of proposed model with different existing methods

From the above-mentioned results, it is ensured that the presented model is found to be an effective tool for the 3D visualization and volume measurement of lung tumor. Therefore, it can be employed by physicians during the surgical process.

Conclusion

This paper has developed an efficient automated 3D lung cancer tumor visualization and volume measurement technique using Simpleware Synopsys software. The presented model utilizes the Simpleware Synopsys software to visualize the tumor in 3D format and measure the tumor size. The set of processes used in the applied software are MF based pre-processing, region growing

Annals of R.S.C.B., ISSN: 1583-6258, Vol. 25, Issue 1, 2021, Pages. 6096 - 6110
Received 15 December 2020; Accepted 05 January 2021.

based segmentation, morphological operations, smoothing, cavity filling, fill gaps, island removal, and local surface correction. For assessing the proficient results of the presented model, a series of simulations were performed on LIDC dataset and our own dataset collected from JIPMER hospital, Puducherry. India. The simulation outcome ensured the superior performance of the presented model by obtaining a maximum accuracy of 98%. As a part of future scope, the presented model can be extended to 3D modelling for other organs.

References

[1] GLOBOCAN 2012 v1.0: cancer incidence and mortality worldwide: IARC CancerBase no. 11. Lyon, France: International Agency for Research on Cancer, 2013 (http://globocan.iarc.fr).

[2] Schwartz A, Cote M. Epidemiology of lung cancer. In: Ahmad A, Gadgeel SM, eds. Lung cancer and personalized medicine: current knowledge and therapies. New York: Springer, 2016:21-41.

[3] Islam S, Walker RC. Advanced imaging (positron emission tomography and magnetic resonance imaging) and imageguided biopsy in initial staging and monitoring of therapy of lung cancer. Cancer J 2013;19:208-16.

[4] D. Cascio, R. Magro, F. Fauci, M. Iacomi, and G. Raso, ‘‘Automatic detection of lung nodules in CT datasets based on stable 3D mass–spring models,’’ Comput. Biol. Med., vol. 42, no. 11, pp. 1098–1109, Nov. 2012.

[5] F. Shariaty and M. Mousavi, ‘‘Application of CAD systems for the automatic detection of lung nodules,’’ Informat. Med. Unlocked, vol. 15, Apr. 2019, Art. no. 100173.

[6] G. Y. Zheng, X. B. Liu, and G. H. Han, ‘‘Survey on medical image computer aided detection and diagnosis systems,’’ J. Softw., vol. 29, no. 5, pp. 1471–1514, 2018.

[7] K. He, X. Zhang, S. Ren, and J. Sun, ‘‘Delving deep into rectifiers: Surpassing human-level performance on ImageNet classification,’’ in Proc. IEEE Int. Conf. Comput. Vis. (ICCV), Santiago, Chile, Dec. 2015, pp. 1026–1034.

[8] A. A. A. Setio, F. Ciompi, G. Litjens, P. Gerke, C. Jacobs, S. J. van Riel, M. M. W. Wille, M. Naqibullah, C. I. Sanchez, and B. van Ginneken, ‘‘Pulmonary nodule detection in CT images: False positive reduction using multi-view convolutional networks,’’ IEEE Trans. Med. Imag., vol. 35, no. 5, pp. 1160–1169, May 2016.

[9] A. A. A. Setio et al., ‘‘Validation, comparison, and combination of algorithms for automatic detection of pulmonary nodules in computed tomography images: The LUNA16 challenge,’’ Med. Image Anal., vol. 42, pp. 1–13, Dec. 2017.

[10] P. Sarker, M. M. H. Shuvo, Z. Hossain, and S. Hasan, ‘‘Segmentation and classification of lung tumor from 3D CT image using K-means clustering algorithm,’’ in Proc. 4th Int. Conf. Adv. Elect. Eng. (ICAEE), Shenzhen, China, Sep. 2017, pp. 731–736.

[11] K. He, G. Gkioxari, P. Dollar, and R. Girshick, ‘‘Mask R-CNN,’’ in Proc. IEEE Int. Conf. Comput. Vis. (ICCV), Venice, Italy, Oct. 2017, pp. 2961–2969.

Annals of R.S.C.B., ISSN: 1583-6258, Vol. 25, Issue 1, 2021, Pages. 6096 - 6110
Received 15 December 2020; Accepted 05 January 2021.

[12] X. Zhang, G. An, and Y. Liu, ‘‘Mask R-CNN with feature pyramid attention for instance segmentation,’’ in Proc. 14th IEEE Int. Conf. Signal Process. (ICSP), Bengaluru, India, Aug. 2018, pp. 1194–1197.

[13] S. Soltaninejad, M. Keshani, and F. Tajeripour, ‘‘Lung nodule detection by KNN classifier and active contour modelling and 3D visualization,’’ in Proc. 16th CSI Int. Symp. Artif. Intell. Signal Process. (AISP), Fars, Iran, May 2012, pp. 440–445.

[14] M. Levoy, ‘‘Display of surfaces from volume data,’’ IEEE Comput. Graph. Appl., vol. 8, no. 3, pp. 29–37, May 1988.

[15] Y. Zhang, P. Gao, and X.-Q. Li, ‘‘A novel parallel ray-casting algorithm,’’ in Proc. 13th Int. Comput. Conf. Wavelet Act. Media Technol. Inf. Process. (ICCWAMTIP), Chengdu, China, Dec. 2016.

[16] Kavitha, M.S., Shanthini, J. and Karthikeyan, N, “Volumetric analysis framework for accurate segmentation and classification (VAF-ASC) of lung tumor from CT images” vol.24, pp:18489–18497, Springer, Soft Computing, June 2020.

[17] https://wiki.cancerimagingarchive.net/display/Public/LIDC-IDRI